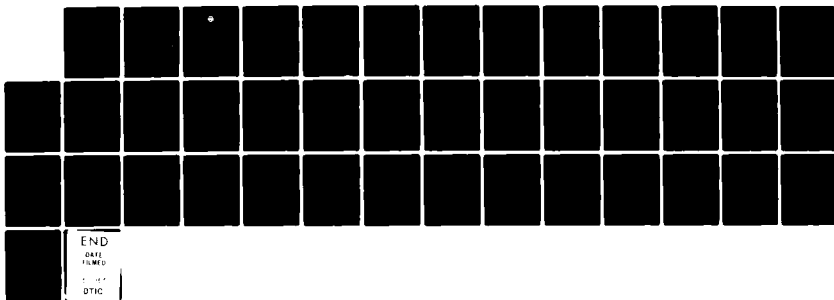


AD-A124 375 PROCESSING OF DIGITAL IONOGRAMS(U) NAVAL OCEAN SYSTEMS 1/1
CENTER SAN DIEGO CA A K PAUL 27 JUL 82 NOSC/TD-529

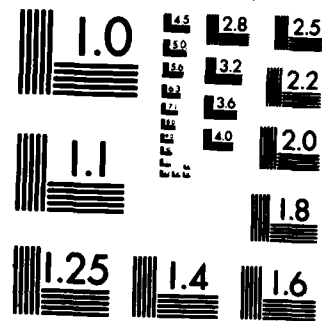
UNCLASSIFIED

F/G 4/1

NL



END
DATE
FILED
DTIC



MICROCOPY RESOLUTION TEST CHART
NATIONAL BUREAU OF STANDARDS-1963-A

102.

Technical Document 529

PROCESSING OF DIGITAL IONOGRAMS

A. K. Paul

27 July 1982

Prepared for
Naval Sea Systems Command

W A 1 2 4 3 7 5



Approved for public release; distribution unlimited

DTIC FILE COPY

NOSC

NAVAL OCEAN SYSTEMS CENTER
San Diego, California 92152

83 02 014 181



NAVAL OCEAN SYSTEMS CENTER, SAN DIEGO, CA 92152

A N A C T I V I T Y O F T H E N A V A L M A T E R I A L C O M M A N D

JM PATTON, CAPT, USN
Commander

HL BLOOD
Technical Director

ADMINISTRATIVE INFORMATION

The work reported here was performed by members of the Ocean and Atmospheric Sciences Division under program element 62759N. Washington sponsorship was provided by the Naval Sea Systems Command.

Released by
J.H. Richter, Head
Ocean and Atmospheric
Sciences Division

Under authority of
J.D. Hightower, Head
Environmental Sciences
Department

UNCLASSIFIED

SECURITY CLASSIFICATION OF THIS PAGE (When Data Entered)

REPORT DOCUMENTATION PAGE		READ INSTRUCTIONS BEFORE COMPLETING FORM
1. REPORT NUMBER NOSC Technical Document 529 (TD 529)	2. GOVT ACCESSION NO. A124 373	3. RECIPIENT'S CATALOG NUMBER
4. TITLE (and Subtitle) PROCESSING OF DIGITAL IONOGRAMS	5. TYPE OF REPORT & PERIOD COVERED	
7. AUTHOR(s) A.K. Paul	8. PERFORMING ORG. REPORT NUMBER	
9. PERFORMING ORGANIZATION NAME AND ADDRESS Naval Ocean Systems Center San Diego, CA 92152	10. PROGRAM ELEMENT, PROJECT, TASK AREA & WORK UNIT NUMBERS 62759N	
11. CONTROLLING OFFICE NAME AND ADDRESS Naval Sea Systems Command Washington DC 20362	12. REPORT DATE 27 July 1982	
14. MONITORING AGENCY NAME & ADDRESS(if different from Controlling Office)	13. NUMBER OF PAGES 36	
16. DISTRIBUTION STATEMENT (of this Report) Approved for public release; distribution unlimited	15. SECURITY CLASS. (of this report) Unclassified	
17. DISTRIBUTION STATEMENT (of the abstract entered in Block 20, if different from Report)	15a. DECLASSIFICATION/ DOWNGRADING SCHEDULE	
18. SUPPLEMENTARY NOTES		
19. KEY WORDS (Continue on reverse side if necessary and identify by block number) Ionogram Doppler velocity F-region peak fitting	Echolocation Mode separation Propagation parameter	
20. ABSTRACT (Continue on reverse side if necessary and identify by block number) More precise and more complete (amplitude and phase) information can be obtained with modern digital ionosondes. This in turn stimulated the development of new data processing routines which can provide new and better information about the ionosphere. The mathematical principles of computing angle of arrival (echolocation), Doppler velocity, and more accurate virtual heights; separating overlapping ordinary and extraordinary echos; estimating peak parameters; etc are described together with some applications and first steps toward automatic scaling of ionograms.		

UNCLASSIFIED

SECURITY CLASSIFICATION OF THIS PAGE (When Data Entered)

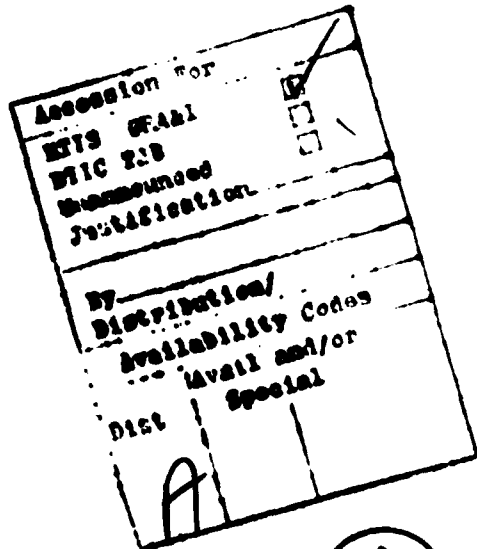
S/N 0102-LF-014-6601

UNCLASSIFIED

SECURITY CLASSIFICATION OF THIS PAGE (When Data Entered)

CONTENTS

INTRODUCTION.....	1
THE DATA.....	1
The Information Content of the Pulse.....	2
Angle of Arrival.....	5
DOPPLER FREQUENCY AND VELOCITY.....	6
Group Path.....	7
Polarization Discrimination.....	9
Separation of Overlapping Ordinary and Extraordinary Echoes.....	9
THE MUF(3000).....	20
F Region Peak Parameters.....	22
Absorption Measurements.....	26
CONCLUSIONS.....	27
REFERENCES.....	31



INTRODUCTION

Modern digital ionosondes provide many new opportunities in ionospheric observations and promise significant progress in understanding the dynamic processes in the ionosphere. The capabilities and sensitivity of digital ionosondes will be demonstrated by using the NOAA ionosonde (Grubb, R. N., 1979) as a prototype example. The emphasis will be on the mathematical principles of ionogram processing, which will be applicable to most digital ionograms depending on their design and mode of operation. At the same time, this report may give some guidance for the design of new digital ionosondes, depending on the user's needs.

THE DATA

Ionograms obtained with classical ionosondes produced a display of the travel times or virtual heights of echoes as a function of frequency. Both the frequency and the virtual heights were defined in some analog fashion and were of limited accuracy. Modern digital ionosondes derive the frequencies from a frequency synthesizer with very high precision and also measure the amplitude and phase of each echo in addition to the virtual heights. As we will see later, it is especially this phase which provides new and more accurate information. In a typical mode of operation, the NOAA ionosonde has four short dipoles as receiving antennas located in the corners of a square and oriented along the diagonals of the square. A two-channel quadrature receiver is connected to one or other diagonal antenna pair during one

transmit-receive cycle. A full data set is obtained by transmitting four pulses, two at a frequency f and two at a slightly higher frequency $f + \Delta f$, where Δf is kept constant through the frequency sweep and is usually 8 kHz. Such a set then gives virtual heights, the quadrature components equivalent to amplitude and phase for each echo for four antennas and two frequencies. Since the echo detection scheme is based on 10- μ s samples, and differences in travel time of the eight echoes in a set are small compared with the sampling interval, care is taken that the echo information is recorded at the same reference time relative to the pulse transmission closest to the average maximum amplitude.

Phase measurements are accurate to approximately 1° if the signal-to-noise ratio is high. The quadrature components, the output of the linear receiver channels, are digitized to 12-bit numbers (including sign). With each transmitted pulse, a delayed calibration pulse is injected into the preamplifiers at the center of the antenna square, is recorded, and permits correction of possible differences in cable length from antenna to receiver, differences in the preamplifier characteristics, and differences between receiver channels. The noise level is also recorded, averaged over a window between the transmitted pulse and the lowest expected E-region echo. This way, echoes with poor signal-to-noise ratio can be eliminated in the data analysis.

THE INFORMATION CONTENT OF THE PHASE

The phase value ϕ obtained for an individual echo is linearly related to the phase height (or phase integral). The constant term in this relation is

unknown and normally cannot be determined. However, the relation between the variation of the phase with time, frequency, location, and ionospheric parameters is well known. This can be expressed in the following way:

$$d\phi = \frac{\partial \phi}{\partial x} dx + \frac{\partial \phi}{\partial y} dy + \frac{\partial \phi}{\partial t} dt + \frac{\partial \phi}{\partial f} df + d\phi_o. \quad (1)$$

(It is assumed that the four receiving antennas are in one horizontal plane; otherwise, another term for the height variation has to be included.) In this equation, the spatial variation of the phase yields the angle of arrival of the echo; the temporal variation yields the Doppler frequency or Doppler velocity (change of phase height with time); and the variation with frequency gives a more accurate estimate of the virtual height according to the principle of stationary phase. The quantity $d\phi_o$ accounts for the difference in antenna orientation.

We assume now that one antenna pair is in the north-south direction and the other in the east-west direction, and label the antennas N, E, S, W. We further use a cartesian coordinate system with the x-axis pointing east and the y-axis pointing north, and its center in the center of the antenna square. To separate the several phase variations, we use the following antenna frequency switching sequence:

1	N, S f	ϕ_{N1}, ϕ_{S1}
2	E, W f	ϕ_{E1}, ϕ_{W1}
3	E, W $f+\Delta f$	ϕ_{E2}, ϕ_{W2}
4	N, S $f+\Delta f$	ϕ_{N2}, ϕ_{S2}

(More sophisticated antenna frequency switching sequences were suggested by Wright, Pitteway et al, 1982). We now assume that D is the length of the diagonal of the antenna square and Δt the time interval between consecutive pulses. It is now easy to derive the following set of equations:

$$\phi_{E1} - \phi_{W1} = D \frac{\partial \phi}{\partial x}$$

$$\phi_{E2} - \phi_{W2} = D \frac{\partial \phi}{\partial x}$$

$$\phi_{N1} - \phi_{S1} = D \frac{\partial \phi}{\partial y}$$

$$\phi_{N2} - \phi_{S2} = D \frac{\partial \phi}{\partial y} \quad (2)$$

$$\phi_{N2} - \phi_{N1} - (\phi_{E2} - \phi_{E1}) = 2 \Delta t \frac{\partial \phi}{\partial t}$$

$$\phi_{S2} - \phi_{S1} - (\phi_{W2} - \phi_{W1}) = 2 \Delta t \frac{\partial \phi}{\partial t}$$

$$3 (\phi_{E2} - \phi_{E1}) - (\phi_{N2} - \phi_{N1}) = 2 \Delta f \frac{\partial \phi}{\partial f}$$

$$3 (\phi_{W2} - \phi_{W1}) - (\phi_{S2} - \phi_{S1}) = 2 \Delta f \frac{\partial \phi}{\partial f}$$

Each of the unknowns in this set of equations can be obtained by two independent combinations of two or four measured phase values. The simplest solution is to take the mean value as the result for each unknown and the mean difference as an error estimate. The same mean values are obtained in a least-squares fit if we consider the measured phase values as deviations from

a fictitious phase value for the center of the 4-dimensional box (x, y, t, f).

Before discussing the phase deviations in more detail, it is important to remember the relation between the phase ϕ and the phase path p^* . The phase path p^* is defined by:

$$p^* = \int \mu ds \quad (3)$$

where μ is the phase refractive index and ds the path element. On the other hand, we have:

$$p^* = \frac{\lambda}{2\pi} \phi \quad (4)$$

or $\phi = \frac{2\pi}{c} f p^*.$ (5)

ANGLE OF ARRIVAL

Outside the ionosphere, $\mu=1$ and $\text{grad } p^*$ according to (3) is a unit vector pointing in the direction of propagation; in other words, the z-component of $\text{grad } p^*$ is negative for an echo reflected from the ionosphere. We obtain $\frac{\partial p^*}{\partial x}$ and $\frac{\partial p^*}{\partial y}$ from (2) and (4) and have, therefore,

$$\frac{\partial p^*}{\partial z} = - [1 - (\frac{\partial p^*}{\partial x})^2 - (\frac{\partial p^*}{\partial y})^2]^{1/2}. \quad (6)$$

The direction toward the apparent reflection point in the ionosphere is then given by a unit vector \bar{w} with

$$\bar{w} \cdot (w_x, w_y, w_z) = - \text{grad } p^*. \quad (7)$$

The zenith distance ξ and the azimuth angle α (measured from east over north consistent with the cartesian coordinate system) are then given by

$$\xi = \arcsin (\sqrt{w_x^2 + w_y^2}) \quad (8)$$

$$\cos \alpha = w_x / \sqrt{w_x^2 + w_y^2} \quad (9)$$

$$\sin \alpha = w_y / \sqrt{w_x^2 + w_y^2}.$$

DOPPLER FREQUENCY AND VELOCITY

From (2), we obtain the change of phase with time and can define a Doppler frequency f_d by

$$f_d = \frac{1}{2\pi} \frac{\partial \phi}{\partial t}. \quad (10)$$

In many cases, it may be more interesting to define a Doppler velocity v_d by

$$v_d = \frac{\partial p^*}{\partial t} = \frac{\lambda}{2\pi} \frac{\partial \phi}{\partial t}. \quad (11)$$

It must be pointed out that v_d in the above definition is the total path change with time. In case of echoes reflected from a layer moving as a whole, one-half the velocity defined above would be the true velocity of the motion of the layer. In this case, the velocity would be constant for all frequencies reflected from such a moving layer, while the Doppler frequency would increase proportional with the radio frequency. Since the phase path is

increasing when the distance to the layer increases, the Doppler velocity will be positive and, correspondingly, the velocity will be negative when the distance decreases. The interpretation of such a velocity is not always simple. For example, assume that the electron density locally increases somewhere along the path without any change near or at the reflection level. In this case the phase path decreases, the group path increases, and the true path length is unchanged (Paul et al, 1974).

A typical example of this type of measurement is shown in figure 1. The data were taken during the sunrise period on 8 January 1981 at Brighton, Colorado, and the results shown were derived as averages over three consecutive frequencies near the F-region peak. Ordinary and extraordinary echoes were analyzed separately at corresponding frequencies and are marked by o and x in the plot. The echoes came approximately from southeast as expected, and approximately 10° off vertical. The Doppler velocity of -50 m/s is of course related to the velocity with which the ionization front approaches. The lowest part of figure 1 shows the deviation of the MUF (3000) from the rapid linear increase of this quantity (to be discussed later), indicating some disturbance by gravity waves which is also visible in the temporal variation of the other quantities shown. The close agreement between ordinary and extraordinary results indicates a high reliability of the data and their analysis.

GROUP PATH

According to the principle of stationary phase, the group path p' and phase path p^* are related in the following way:

$$p' = \frac{d}{df} (fp^*) = \frac{c}{2\pi} \frac{d\phi}{df} \quad (12)$$

where c is the velocity of light.

For vertical reflection, the corresponding relation between virtual height h' and phase height h^* is valid. With (12) we have the possibility of measuring the virtual height or group path independently from the measurement of the travel time. Obtaining the travel time means first selecting a certain characteristic of the shape of the transmitted pulse (leading edge, steepest slope, maximum amplitude, etc) which is also expected to be found in the reflected echo. The time difference between the appearance of this characteristic in the transmitted and reflected pulse is then the travel time. This procedure has limited accuracy, since the pulse shape can be distorted between transmission and reception (Paul, 1979). In general, the phase is less sensitive to distortion and the phase change over a small frequency interval gives a more accurate estimate of the group path or virtual height. The phase may change by several full rotations plus a fraction of a rotation over a given frequency interval. Only the fraction is obtained by the phase comparison, and the number of full rotations has to be determined from the travel time.

The frequency increment $\Delta f = 8$ kHz corresponds to a basic virtual height unit of 18.75 km for one full phase rotation. If phase changes over this frequency interval can be measured with an accuracy of 1° , the resulting virtual heights have an accuracy of about 50 m. For a smaller Δf and the same phase resolution, the accuracy of the virtual heights would decrease. On the other hand, for a virtual height of 300 km, the phase changes by 16 full rota-

tions over the frequency interval of 8 kHz and a much larger value of Δf may cause difficulties in determining the number of full rotations unambiguously. In addition, for a large Δf the linear approximation of the phase variation in the frequency becomes inaccurate and a higher-order function for ϕ (f) would have to be used in the analysis.

POLARIZATION DISCRIMINATION

Assume that ordinary and extraordinary echoes at a given frequency are well separated in virtual heights. The phases of the north-south antenna pair then should be different from phases at the east-west pair by $d\phi_o = + 90^\circ$ or $d\phi_o = - 90^\circ$, depending on the sense of rotation [see equation (1)]. For the purposes of identifying an echo as ordinary or extraordinary it is not necessary to solve for $d\phi_o$. Comparing the mean phase values of the north-south pair with the mean phase value of the east-west pair, we have the one or other component, depending on whether the phase difference is close to $+90^\circ$ or close to -90° . This is still true if the pulse is reflected obliquely.

SEPARATION OF OVERLAPPING ORDINARY AND EXTRAORDINARY ECHOES

In most ionograms, there are some frequency ranges where ordinary and extraordinary echoes have approximately equal travel times and the two traces cross each other. If the two echoes overlap sufficiently, we obtain an interference pattern as a function of frequency and the distinction between the two modes in terms of travel time is no longer possible. The resulting sequence of maxima and minima as a function of frequency is not in phase at the four receiving antennas except that both echoes are returned exactly vertically.

If amplitude and phase at each of the four antennas are recorded for a given frequency, the separation of the two echoes is possible under rather general conditions.

It is assumed that the two components are circularly polarized with opposite sense of rotation. They will appear to be elliptically polarized, if they are not reflected vertically. As mentioned earlier, the apparent direction to the reflection point can be described by the zenith distance ξ and the azimuth angle α and the components of the unit vector \bar{w} in (7) are then given by:

$$\bar{w} = [\sin \xi \cos \alpha, \sin \xi \sin \alpha, \cos \xi]. \quad (13)$$

The electric vector is perpendicular to \bar{w} , and a unit vector \bar{e} in the direction of the electric vector must satisfy the following conditions:

$$e_x^2 + e_y^2 + e_z^2 = 1 \quad (14)$$

$$\text{and } e_x w_x + e_y w_y + e_z w_z = 0. \quad (15)$$

At an instant when the electric vector is in the (y, z) plane, we have with (13), (14), and (15),

$$\bar{e}_N = [0, \cos \xi / sc, \sin \xi \sin \alpha / sc] \quad (16)$$

with

$$sc = (1 - \sin^2 \xi \cos^2 \alpha)^{1/2}. \quad (17)$$

When \mathbf{e} is in the (x, z) plane, we have

$$\mathbf{e}_E = [\cos \xi/ss, 0, \sin \xi \cos \alpha/ss] \quad (18)$$

with

$$ss = (1 - \sin^2 \xi \sin^2 \alpha)^{1/2}. \quad (19)$$

The amplitude observed at the north and south antenna (oriented in the north-south direction) would then be proportional to \mathbf{e}_y in (16) and the amplitude observed at the east and west antenna would be proportional to \mathbf{e}_x in (18) with the same proportionality factor. In other words, the amplitude ratio r_a between the north-south and the east-west antenna pairs is given by:

$$r_a = ss/sc. \quad (20)$$

Corresponding to the off vertical incidence of an echo, we observe a phase difference between the north and south antenna and also between the east and west antenna. Those phase differences are proportional to \mathbf{e}_z in (16) and (18) respectively. Defining $\Delta\phi_N$ as the phase difference between the north antenna and a fictitious antenna in the center of the array, and correspondingly a phase difference $\Delta\phi_E$, we have

$$\Delta\phi_N = -\frac{\pi D}{\lambda} \sin \xi \sin \alpha/sc \quad (21)$$

and $\Delta\phi_E = -\frac{\pi D}{\lambda} \sin \xi \cos \alpha/ss \quad (22)$

where λ is the radio wavelength and D is the diagonal distance between antenna pairs as in (2).

We now can write the equations for the quadrature components of two overlapping echoes with their electric vectors rotating in opposite directions, neglecting temporal variation over the interval of two consecutive pulses. We use the symbols $a, \epsilon_N, b, \epsilon_E$ for amplitude and phase difference on the north and east antenna for one component and b, δ_N, d, δ_E correspondingly for the other component. The phases of the two components for the center of the array are described by ϕ_1 and ϕ_2 . The indices X and Y indicate the cosine and sine term of the quadrature component, while the symbols N, E, S, and W are used for the magnitude of the quadrature components at the four antennas.

$$N_X = a \cos (\phi_1 + \epsilon_N) + b \cos (\phi_2 + \delta_N)$$

$$N_Y = a \sin (\phi_1 + \epsilon_N) + b \sin (\phi_2 + \delta_N)$$

$$E_X = -c \sin (\phi_1 + \epsilon_E) + d \sin (\phi_2 + \delta_E)$$

$$E_Y = c \cos (\phi_1 + \epsilon_E) - d \cos (\phi_2 + \delta_E)$$

$$S_X = a \cos (\phi_1 - \epsilon_N) + b \cos (\phi_2 - \delta_N)$$

$$S_Y = a \sin (\phi_1 - \epsilon_N) + b \sin (\phi_2 - \delta_N)$$

$$W_X = -c \sin (\phi_1 - \epsilon_E) + d \sin (\phi_2 - \delta_E)$$

(23)

$$w_y = c \cos(\phi_1 - \epsilon_E) - d \cos(\phi_2 - \delta_E).$$

These are eight equations for 10 unknowns. In addition, we have according to (20),

$$\frac{a}{c} = ss_1/sc_1, \quad (24)$$

where ss_1 and sc_1 are the quantities defined in (17) and (19) for ξ_1 and α_1 , the zenith distance and azimuth for one component; according to (21) and (22),

$$\epsilon_N = -\pi \frac{D}{\lambda} \sin \xi_1 \sin \alpha_1 / sc_1, \quad (25)$$

$$\epsilon_E = -\pi \frac{D}{\lambda} \sin \xi_1 \cos \alpha_1 / ss_1.$$

The corresponding set of equations for the other component is then

$$\frac{b}{d} = ss_2/sc_2 \quad (26)$$

$$\delta_N = -\pi \frac{D}{\lambda} \sin \xi_2 \sin \alpha_2 / sc_2 \quad (27)$$

$$\delta_E = -\pi \frac{D}{\lambda} \sin \xi_2 \cos \alpha_2 / ss_2.$$

Equations (24)-(27) add six more equations for four more unknowns and we have now 14 equations for 14 unknowns. Unfortunately, those equations are non-linear and do not offer an easy exact solution, if such an exact solution exists at all. In the following, we will show how an approximate solution can be found which can be improved by iteration.

First, we define eight combinations of the quadrature components

$$R_1 = N_X + S_X = 2 a \cos \phi_1 \cos \epsilon_N + 2 b \cos \phi_2 \cos \delta_N$$

$$R_2 = N_X - S_X = -2 a \sin \phi_1 \sin \epsilon_N - 2 b \sin \phi_2 \sin \delta_N$$

$$R_3 = N_Y + S_Y = 2 a \sin \phi_1 \cos \epsilon_N + 2 b \sin \phi_2 \cos \delta_N$$

$$R_4 = N_Y - S_Y = 2 a \cos \phi_1 \sin \epsilon_N + 2 b \cos \phi_2 \sin \delta_N \quad (28)$$

$$R_5 = E_X + W_X = -2 c \sin \phi_1 \cos \epsilon_E + 2 d \sin \phi_2 \cos \delta_E$$

$$R_6 = E_X - W_X = -2 c \cos \phi_1 \sin \epsilon_E + 2 d \cos \phi_2 \sin \delta_E$$

$$R_7 = E_Y + W_Y = 2 c \cos \phi_1 \cos \epsilon_E - 2 d \cos \phi_2 \cos \delta_E$$

$$R_8 = E_Y - W_Y = -2 c \sin \phi_1 \sin \epsilon_E + 2 d \sin \phi_2 \sin \delta_E.$$

We now use the following identities

$$2 a = a + c + (a - c)$$

$$2 c = a + c - (a - c)$$

$$2 b = b + d + (b - d)$$

$$2d = b + d - (b - d)$$

and define

$$T_1 = R_1 - (a-c) \cos \phi_1 \cos \epsilon_N - (b-d) \cos \phi_2 \cos \delta_N$$

$$T_2 = R_2 + (a-c) \sin \phi_1 \sin \epsilon_N + (b-d) \sin \phi_2 \sin \delta_N$$

$$T_3 = R_3 - (a-c) \sin \phi_1 \cos \epsilon_N - (b-d) \sin \phi_2 \cos \delta_N$$

$$T_4 = R_4 - (a-c) \cos \phi_1 \sin \epsilon_N - (b-d) \cos \phi_2 \sin \delta_N \quad (29)$$

$$T_5 = R_5 + (a-c) \sin \phi_1 \cos \epsilon_E - (b-d) \sin \phi_2 \cos \delta_E$$

$$T_6 = R_6 + (a-c) \cos \phi_1 \sin \epsilon_E - (b-d) \cos \phi_2 \sin \delta_E$$

$$T_7 = R_7 - (a-c) \cos \phi_1 \cos \epsilon_E + (b-d) \cos \phi_2 \cos \delta_E$$

$$T_8 = R_8 + (a-c) \sin \phi_1 \sin \epsilon_E - (b-d) \sin \phi_2 \sin \delta_E.$$

According to (28), the equation system (29) is equivalent to

$$T_1 = (a+c) \cos \phi_1 \cos \epsilon_N + (b+d) \cos \phi_2 \cos \delta_N$$

$$T_2 = -(a+c) \sin \phi_1 \sin \epsilon_N - (b+d) \sin \phi_2 \sin \delta_N$$

$$T_3 = (a+c) \sin \phi_1 \cos \epsilon_N + (b+d) \sin \phi_2 \cos \delta_N$$

$$T_4 = (a+c) \cos \phi_1 \sin \epsilon_N + (b+d) \cos \phi_2 \sin \delta_N \quad (30)$$

$$T_5 = -(a+c) \sin \phi_1 \cos \epsilon_E + (b+d) \sin \phi_2 \cos \delta_E$$

$$T_6 = -(a+c) \cos \phi_1 \sin \epsilon_E + (b+d) \cos \phi_2 \sin \delta_E$$

$$T_7 = (a+c) \cos \phi_1 \cos \epsilon_E - (b+d) \cos \phi_2 \cos \delta_E$$

$$T_8 = -(a+c) \sin \phi_1 \sin \epsilon_E + (b+d) \sin \phi_2 \sin \delta_E.$$

Using the symbols

$$s_1 = \sin \phi_1$$

$$c_1 = \cos \phi_1$$

$$s_2 = \sin \phi_2$$

$$c_2 = \cos \phi_2$$

we derive from (30)

$$s_1 T_1 - c_1 T_3 = -(b+d) \sin (\phi_2 - \phi_1) \cos \delta_N$$

$$s_1 T_4 + c_1 T_2 = -(b+d) \sin (\phi_2 - \phi_1) \sin \delta_N \quad (31)$$

$$s_1 T_7 + c_1 T_5 = (b+d) \sin (\phi_2 - \phi_1) \cos \delta_E$$

$$S_1 T_6 - C_1 T_8 = -(b+d) \sin(\phi_2 - \phi_1) \sin \epsilon_E$$

and

$$S_2 T_1 - C_2 T_3 = (a+c) \sin(\phi_2 - \phi_1) \cos \epsilon_N$$

$$S_2 T_4 + C_2 T_2 = (a+c) \sin(\phi_2 - \phi_1) \sin \epsilon_N \quad (32)$$

$$S_2 T_7 + C_2 T_5 = (a+c) \sin(\phi_2 - \phi_1) \cos \epsilon_E$$

$$S_2 T_6 - C_2 T_8 = -(a+c) \sin(\phi_2 - \phi_1) \sin \epsilon_E.$$

We now obtain from (31)

$$(S_1 T_1 - C_1 T_3)^2 + (S_1 T_4 + C_1 T_2)^2 = (S_1 T_7 + C_1 T_5)^2 + (S_1 T_6 - C_1 T_8)^2 \quad (33)$$

and a similar equation from (32) with the only difference that S_1 and C_1 are replaced by S_2 and C_2 respectively. In general, we can write instead of (33)

$$S^2(T_1^2 + T_4^2 - T_6^2 - T_7^2) - 2SC(T_1 T_3 - T_2 T_4 + T_5 T_7 - T_6 T_8) + C^2(T_2^2 + T_3^2 - T_5^2 - T_8^2) = 0 \quad (34)$$

If we know the T_i , $i = 1, 8$ and assume that $C \neq 0$ we can derive from (34) a quadratic equation for S/C and its roots are $\tan \phi_1$ and $\tan \phi_2$.

We see now how an iteration process can be formed. In a first step, we assume that the zenith angles are relatively small

$$\sin^2 \xi_i \ll 1 \quad i = 1, 2 \quad (35)$$

which means, according to (17), (19), and (20), that

$a \approx c$ and $b \approx d$;

in other words we neglect terms with factors $(a - c)$ and $(b - d)$ in (29), and have

$$T_i = R_i \quad i = 1, 2, \dots, 8,$$

and obtain $\operatorname{tg} \phi_1$ and $\operatorname{tg} \phi_2$ from (34). Unfortunately this means an ambiguity in ϕ_1 and ϕ_2 by $\pm \pi$. This will be discussed later. Knowing ϕ_1 and ϕ_2 , we obtain δ_N from the first pair of equations in (31), δ_E from the second pair, and $b + d$ from either one pair. Correspondingly we obtain ϵ_N , ϵ_E and $a + c$ from (32).

Now assume that we change ϕ_1 by π . We see that this would cause a change of the sign on the left and right side of all equations in (31), and therefore δ_N and δ_E remain unchanged; while in all equations (32), only the right side would change the sign which has to be compensated by changing ϵ_N and ϵ_E by π . Similarly, a change of ϕ_2 by π would cause a change of δ_N and δ_E by π and leave ϵ_N and ϵ_E unchanged. If ϕ_1 and ϕ_2 are changed by π , all four phase differences δ_N , δ_E , ϵ_N , and ϵ_E have to be changed by π . With the reasonable restriction that δ_N , δ_E , ϵ_N , and ϵ_E are all to be within $\pm \pi/2$, we can eliminate in most cases the ambiguities in ϕ_1 and ϕ_2 . This restriction is consistent with the assumption of small zenith distances, at least for low frequencies. For higher frequencies, $D/\lambda > 1$, the

quantities δ_N , δ_E , ϵ_N , and ϵ_E can become relatively large even for small values of ξ ; here, continuity with frequency can be used to resolve the ambiguities.

Knowing ϵ_N , ϵ_E and $a + c$ and using

$$u = \epsilon_N \frac{\lambda}{\pi D}$$

$$v = \epsilon_E \frac{\lambda}{\pi D} \quad (36)$$

$$w = a + c$$

we obtain with (24) and (25),

$$\sin \xi_1 = (u^2 + v^2 - 2u^2 v^2)^{1/2} / (1 - u^2 v^2)^{1/2} \quad (37)$$

$$\sin \alpha_1 = -u (1 - v^2)^{1/2} / (u^2 + v^2 - 2u^2 v^2)^{1/2} \quad (38)$$

$$\cos \alpha_1 = -v (1 - u^2)^{1/2} / (u^2 + v^2 - 2u^2 v^2)^{1/2} \quad (39)$$

$$a = w (1 - u^2)^{1/2} / [(1 - v^2)^{1/2} + (1 - u^2)^{1/2}] \quad (40)$$

$$c = w (1 - v^2)^{1/2} / [(1 - v^2)^{1/2} + (1 - u^2)^{1/2}]. \quad (41)$$

Exchanging ϵ_N by δ_N , ϵ_E by δ_E , a by b , c by d , and the index 1 by 2, we obtain the corresponding parameters for the other component from (37)-(41).

We now have a first-order estimate of all unknowns and can improve our estimates of the T_i by subtracting the respective terms from R_i according to (29), and the next iteration can be computed. This process was tested on many simulated and real data and was found to be rapidly convergent. Very often, the first iteration was already sufficient to obtain reasonably accurate results. After convergence of this iteration process has been accomplished for a frequency f , we apply the same procedure to the data at $f + \Delta f$. After the phases for each component at f and $f + \Delta f$ are computed, their virtual heights are then obtained from the phase difference over the frequency interval Δf . An example of this type of analysis is demonstrated in figure 2. The symbol M (mixed) indicates the virtual heights observed by measuring the travel time of the overlapped echoes, while the dots (ordinary component) and the crosses (extraordinary component) are the results of the mode separation process. It should be kept in mind that the nominal pulse duration is 60 μs and the actual pulse duration at the receiver output about 100 μs , corresponding to a pulse length on the virtual height scale of 9 km and 15 km, respectively.

THE MUF(3000)

The maximum usable frequency over a 3000 km path MUF(3000) and its ratio to the ordinary critical frequency f_{02} , the propagation factor M(3000) is one of the standard parameters in scaling ionograms. Instead of the table published by URSI (Piggot, W.R., and K. Rawer, 1972), we use an empirical algebraic expression for the MUF function which fits the tabulated values closely (better than 0.5% in the range $200 < h' < 600$ km). We define the MUF

function

$$r = f (3.383 - 0.298 h_r') / \sqrt{h_r'} \quad (42)$$

where f is the radio frequency and h_r' is the relative virtual height of the ordinary component normalized to 400 km:

$$h_r' = h_o' / 400. \quad (43)$$

Without the normalization of h_r' , we have

$$r = f (67.654 - 0.0149 h') / \sqrt{h'}. \quad (44)$$

When r reaches a maximum, its value is then equal to $MUF(3000)$

$$r_{\max} = MUF(3000). \quad (45)$$

If $foF2$ is known, we then obtain

$$M(3000) = MUF(3000) / foF2. \quad (46)$$

Normally, the $MUF(3000)$ is obtained with very high precision, better than $foF2$ or $M(3000)$. Besides its importance for hf communication, the $MUF(3000)$ is very sensitive to natural or artificial disturbances in the F-region and can be used as an indicator for such phenomena. In the numerical process, r is evaluated for a sequence of virtual heights-frequency pairs and the running average over seven values is computed. When this average starts to decrease with increasing frequency, a least squares parabolic fit over the last seven

individual values of r is used to determine r_{\max} , which is equal to the MUF(3000). Figure 3 shows a sequence of MUF(3000) values computed from ionograms taken in 2-minute intervals over a period of about 8 hours. The accuracy and sensitivity of this quantity can better be seen in the insert, where a portion of the same data is displayed on a 5-times-expanded-frequency scale. (Note that each point is obtained independently from one ionogram, and no temporal smoothing, averaging, or filtering was applied.)

F REGION PEAK PARAMETERS

Perhaps the most important parameter obtained by vertical sounding of the ionosphere is the penetration frequency or critical frequency in the ordinary mode f_{0F2} . Actually, it is obtained by extrapolation when the virtual heights as a function of frequency approach infinity. As always, an extrapolated quantity is likely to be less accurate than a direct measurement of an interpolated quantity. This has to be kept in mind when peak parameters, like height of maximum or scale height, are discussed. Even if very precise virtual height and frequencies are available, small disturbances near the F-region peak can cause relatively large errors. It is generally assumed that the F-region peak can be best described by a parabolic model. Under this assumption, it has been shown (Paul et al, 1981) that consecutive frequency differences divided by the corresponding virtual height differences decrease linearly as a function of frequency and their extrapolation to zero gives the critical frequency. This procedure can be used for ordinary and extraordinary mode. We obtain the remaining peak parameters, the height of the maximum h_m and the half thickness y_m (twice the scale height) in the following way. We first calculate parabolic coefficients p_c for the last few frequen-

cies below the critical frequency where virtual heights were observed. Those coefficients, of course, depend on the critical frequency. We then obtain equations of the form

$$h'_i = h_m + (pc_i - 1) y_m \quad (47)$$

Applying the method of least squares to several (5-10) of those equations, we obtain h_m and y_m . An improved estimate of the three peak parameters can be obtained in an iterative least-squares process in which we linearize the dependence of pc on the critical frequency, which can only be done over very small frequency intervals (<50 kHz). This can be important when the peak is slightly distorted (eg, by gravity waves). If fc is the critical frequency (ordinary or extraordinary mode), we write instead of (47)

$$h'_i = h_m + (pc_i + \frac{dpc_i}{dfc} \Delta fc - 1) y_m \quad (48)$$

for the three unknowns h_m , y_m , and Δfc . The quantity Δfc is now a correction to the critical frequency, and the process can be repeated with the new critical frequency. The algorithm for computing the parabolic coefficients will be outlined later.

This method has been applied to hundreds of ionograms and also was tested with simulated data. In most cases, very good agreement between these results and full profile computations was found except in situations where systematic differences were expected, mainly when a very pronounced F1 layer was present and its critical frequency was relatively close to foF2. In those cases, empirical corrections depending on the ratio $foF1/foF2$ can be applied.

Results of those studies will be reported later. If this peak fitting process is applied to ordinary and extraordinary components separately, the differences of the results give some indication of the reliability of the computed parameters.

The peak fitting program together with the MUF(3000) computation can be considered as a first order automatic ionogram processing routine and has been applied directly to many tapes with sequences of 500 and more ionograms without interruptions.

The parabolic coefficients can be computed in the following way. The virtual height h' can be expressed as

$$h' = \int_0^{h_r} \mu' dh \quad (49)$$

where μ' is the group refractive index and h_r is the reflection height. The principle is now to write the identity

$$h' = \int_0^{h_r} \mu' \sqrt{1-x} \frac{1}{\sqrt{1-x}} dh \quad (50)$$

where

$$x = f_N^2/f^2$$

and f_N is the plasma frequency.

The product $\mu' \sqrt{1-x}$ is the ratio of the field included group refractive index to the no-magnetic-field group refractive index, which is easy to evaluate and usually is close to unity. If a closed solution of the virtual height integral for the no-field case is known, we can transform (50) into a Stiltjes integral

$$h' = \int \mu' \sqrt{1-x} d p_n \quad (51)$$

where p_n , the no-field solution, is now used as the integration variable. This is a general principle and can be applied to a variety of other models. In the specific case of a parabolic layer given by

$$f_N^2 = f_c^2 \left[1 - \left(\frac{h-h_m}{y_m} \right)^2 \right] \quad (52)$$

we have for a half thickness of one unit ($y_m = 1$)

$$p_n(x) = \frac{1}{\beta} \ln \frac{1+\beta}{\sqrt{1-x} + \sqrt{\beta^2-x}} \quad (53)$$

with $\beta = f_c/f$

and for the inverse function

$$x = \frac{1}{4} [2(1+\beta^2) - (1+\beta)^2 \exp(-2p_n\beta) - (1-\beta)^2 \exp(2p_n\beta)]. \quad (54)$$

If we divide $p_n(1) - p_n(0)$ by an even number m , we obtain m intervals on the p_n scale. Now we compute the corresponding values of x with (54), evaluate $\mu' \sqrt{1-x}$ for those values of x , and apply Simpson's rule of numerical

integration to obtain the parabolic coefficients.

Results from the peak fitting program are shown in figure 4. Again, ionograms were recorded in 2-minute intervals and each set of peak parameters shown was computed independently from one single ionogram.

ABSORPTION MEASUREMENTS

As mentioned earlier, one data set provides, besides phases and virtual height, eight amplitudes. In most cases, the average over eight amplitudes is significant in the study of systematic variations (eg, absorption as a function of frequency or at a fixed frequency as a function of time). In figure 5, the variation of the absorption with time at a fixed frequency is shown during a solar X-ray flare together with the intensity of X-ray radiation observed from a satellite. All quantities are expressed in dB, with the intensity scale downwards for better comparison. It is interesting to note that at 14h27 the ionospheric absorption is almost back to normal for this particular frequency, while the wideband and narrowband X-ray intensities are still above their reference levels by 20 dB and 60 dB, respectively. These values indicate a threshold which must be exceeded before absorption at this frequency is affected. Approximately the same threshold values are obtained if the data are compared at the onset of the event.

CONCLUSIONS

Some of the algorithms described in this report have been applied and results were published (Wright, J. W., 1982; Wright et al, 1982), while most of the material is new. It is easy to see that modern technology applied in digital ionosondes could open a new area in ionospheric research and hf communications. A few more comments on the figures shown may illustrate this better.

Zenith distances of 10° and more (as shown in figure 1) lasting for approximately 50 minutes are expected to be a regular feature during the sunrise period. Similar effects must exist for the sunset period, probably lasting longer with somewhat smaller zenith angles. On the one hand, more detailed systematic measurements of the apparent echo location, together with the Doppler velocity, could give more insight into the ionization and recombination process in the F-region. On the other hand, the determination of electron density profiles and the height of the F-region maximum becomes an entirely new and more complicated problem under those conditions.

Local F-region tilts corresponding to zenith angles of approximately 10° have a significant effect on hf propagation and cannot be neglected in an hf prediction model. Any attempt of hf direction finding or transmitter location will fail under those conditions.

Sunrise and sunset tilts could be measured and become predictable, and corresponding corrections could be applied to hf prediction models. Tilts of comparable magnitude caused by gravity waves can appear at any time, however, and can have similar effects on hf propagation conditions. The periodicities of these gravity waves are usually somewhat shorter (10-30 minutes; see insert of figure 3) than the duration of sunrise and sunset tilts (40-60 minutes). Gravity waves could become predictable, at least in a statistical sense, if correlations with other geophysical parameters could be established. It should be noted that even weak gravity waves can cause signal distortion and fading in propagation through those areas, and that the quality of signals is inversely related to gravity wave activity.

The increased sensitivity of modern digital ionosondes is best illustrated in figure 3. Changes in the MUF(3000) on the order of 10 kHz are already significant, corresponding to a relative accuracy of the order $5 \cdot 10^{-4}$ for an individual measurement, while the propagation factor $M(3000)$ obtained from analog ionograms is typically accurate to $1.5 \cdot 10^{-2}$ for monthly median values. This high accuracy may not be important for hf propagation, but definitely increases the detectability of natural and artifical disturbances by more than one order of magnitude, provided that the ionogram sequence is fast enough (at least one ionogram every 5 minutes).

Similar comments can be made about the data presented in figure 4. As mentioned earlier, the absolute value of h_m may be influenced by the F1-layer, if present. The periodicities and the magnitudes of the temporal variations visible, however, should be accurate. More tests with simulated data may be required.

The length of the frequency interval in which ordinary and extraordinary components are overlapping depends for a given ionosphere on the pulse length, and can easily be on the order of half the frequency range where echoes are observed. The classical approach to minimize this problem is to keep the pulse length short. Of course, a shorter pulse duration means a wider spectrum, which requires a wider bandwidth of the receiver and more power to maintain a reasonably high signal-to-noise ratio. It also causes poorer accuracy in parts of the ionogram where dispersion becomes significant (Paul, A. K., 1979). Wider bandwidth and higher power of the transmitted pulse causes more interference to other hf users. In general, a pulse duration of 60-100 μ s has become standard. With the solution of the o-x overlap problem, the pulse length could be increased, the pulse power reduced, and the receiver bandwidth made narrower without loss of information at least for F-region observations. For E-region observations, where often small Es patches are embedded in the regular E-region, the two-wave solution (overlap of two echoes with equal polarization) would have to be incorporated in the analysis program if the pulse length were increased.

Besides possible improvements of the instrument, the separation of ordinary and extraordinary components as demonstrated in figure 2. provides a complete echo trace for each component with high accuracy, provided no other disturbance is present (spread F, blanketing Es). This is important for almost every analysis of vertical sounding data, like electron density profiles, gravity waves propagating through the F-region as seen in the angle of arrival, or virtual heights at fixed frequencies as a function of time, ionospheric drift measurements, etc.

The effect of increased absorption caused by solar flares, as shown in figure 5, is well known, but few observations were made measuring the frequencies and time dependence of the absorption and comparing it with X-ray data.

More observations of this kind could at least provide a prediction of the duration of such an absorption event as a function of frequency, depending on the intensity of an observed flare, as long as flares themselves cannot be predicted.

One major advantage of modern digital ionosondes is, of course, the automation of the data analysis. If a minicomputer is part of the system, the analysis could be done in real time. This can be important, where real-time information about the ionosphere is needed (rocket experiments or timing of artificial disturbances). At the same time, real-time processing could eliminate the need of storing the raw data by saving the analyzed results only, which would result in a significant data compression.

It may be added that the savings accomplished by the automatic analysis more than compensates for the higher cost of a modern digital system. In addition, such ionosondes can significantly improve our knowledge about the ionosphere, its physics, and its use as a propagation medium.

REFERENCES

Grubb, R. N., The NOAA SEL HF radar system (Ionospheric Sounder), NOAA Tech Mem ERL SEL-55, 1979.

Paul, A. K., J. W. Wright, and L. S. Fedor, The interpretation of ionospheric drift measurements, VI, angle of arrival and group path (Echolocation) measurements from digitized ionospheric soundings: The Group Path Vector, J Atmos Terr Phys, 36, 721-740, 1974.

Paul, A. K., and D. L. Mackison, Scaling of F-layer critical frequency from digital ionograms applied to observations during the solar eclipse on 26 February 1979, J Atmos Terr Phys, 43, 221-223, 1981.

Paul, A. K., Radio pulse dispersion in the ionosphere, J Geophys 46, 15-21, 1979.

Piggot, W. R., and K. Rawer, URSI handbook of ionogram interpretation and reduction, Report UAG-23, 1972.

Wright, J. W., The application of dopplionograms to an understanding of sporadic E, J Geophys Res 87, 1723-1726, 1982.

Wright, J. W., and M. L. V. Pitteway, Application of dopplionograms and gonionograms to atmospheric gravity wave disturbances in the ionosphere, J Geophys Res 87, 1719-1721, 1982.

Wright, J. W., and M. L. V. Pitteway, Data processing for the dynasonde: The Dopplionogram, J Geophys Res 87, 1589-1598, 1982.

Brighton Jan. 8, 1981

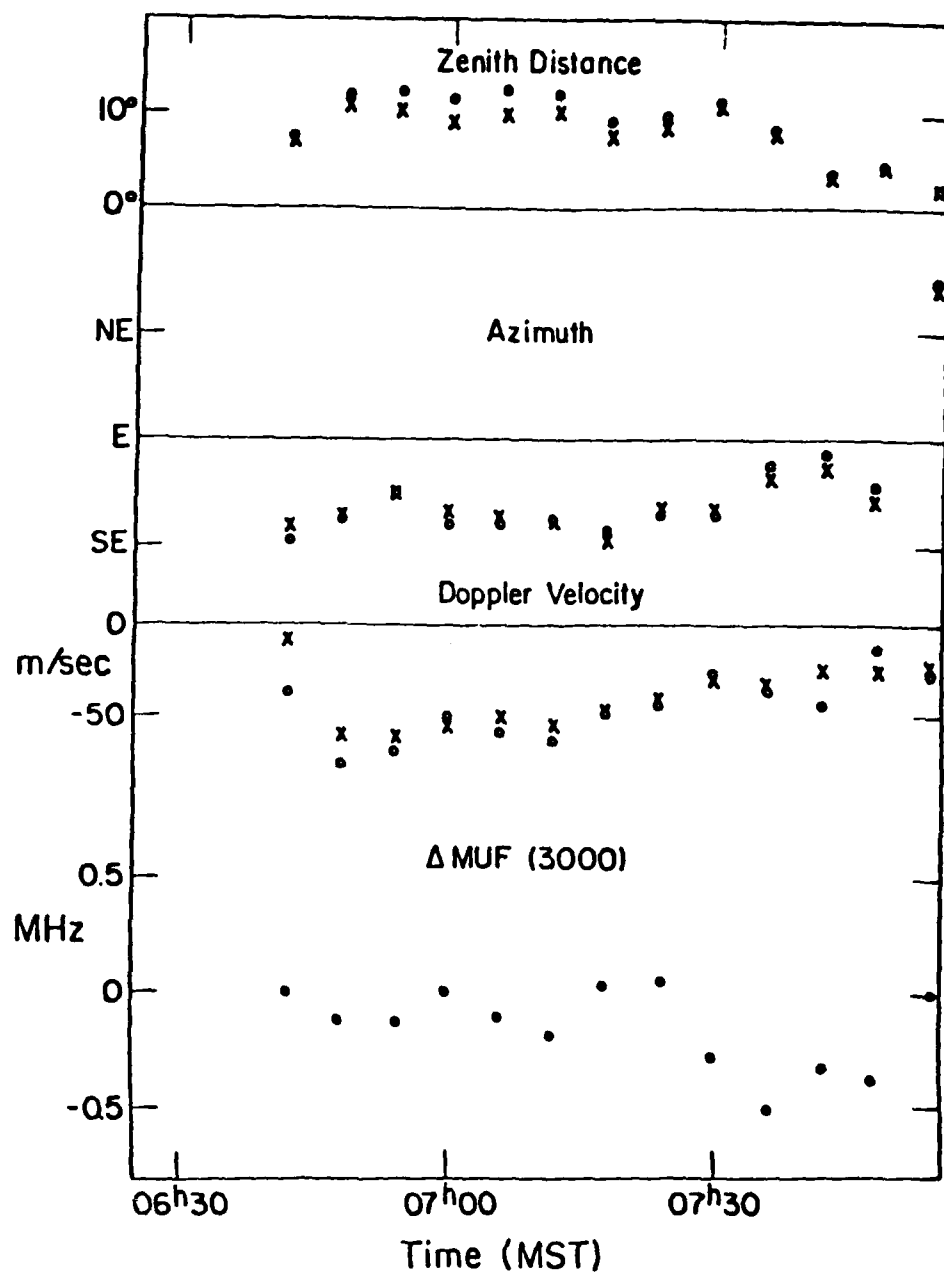


Figure 1. Oblique echoes (angle of arrival), Doppler velocity and MUF (3000) deviation during sunrise period.

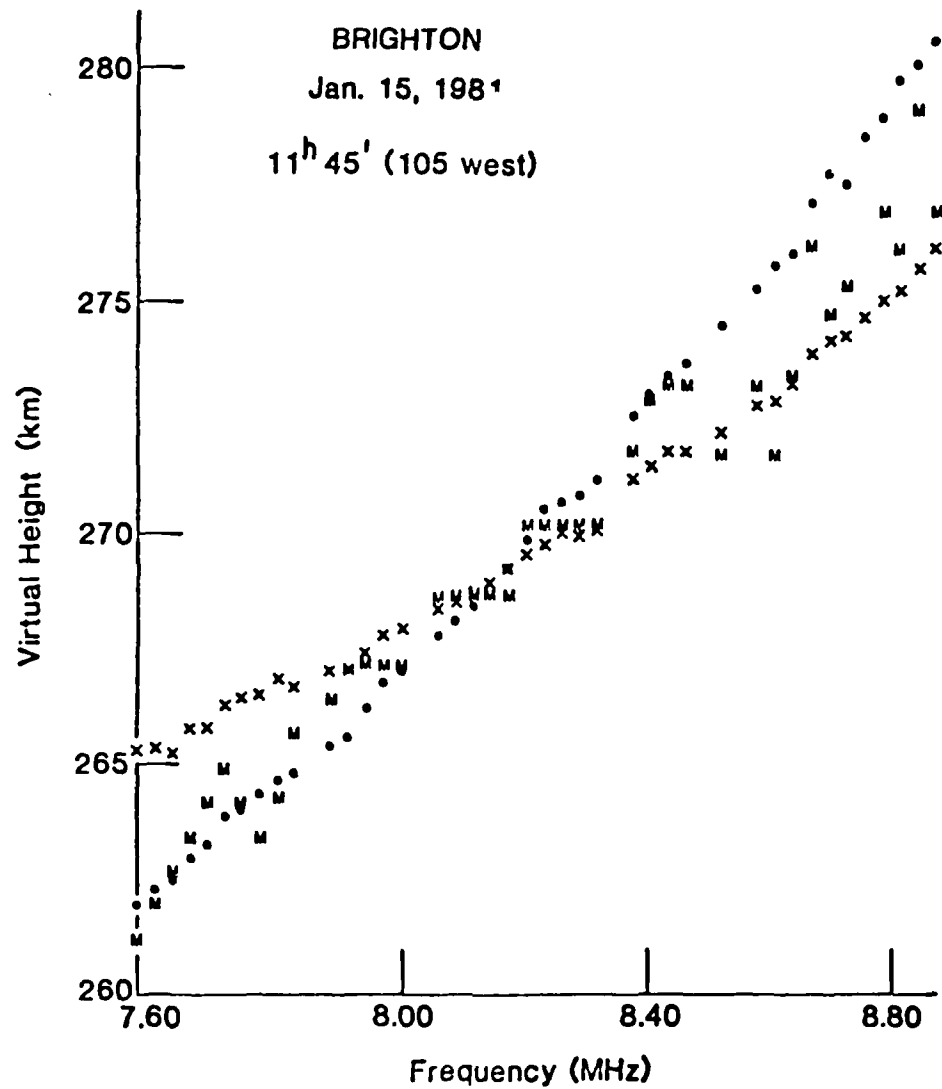


Figure 2. Separation of ordinary (•) and extraordinary (x) echoes from mixed (M) echoes.

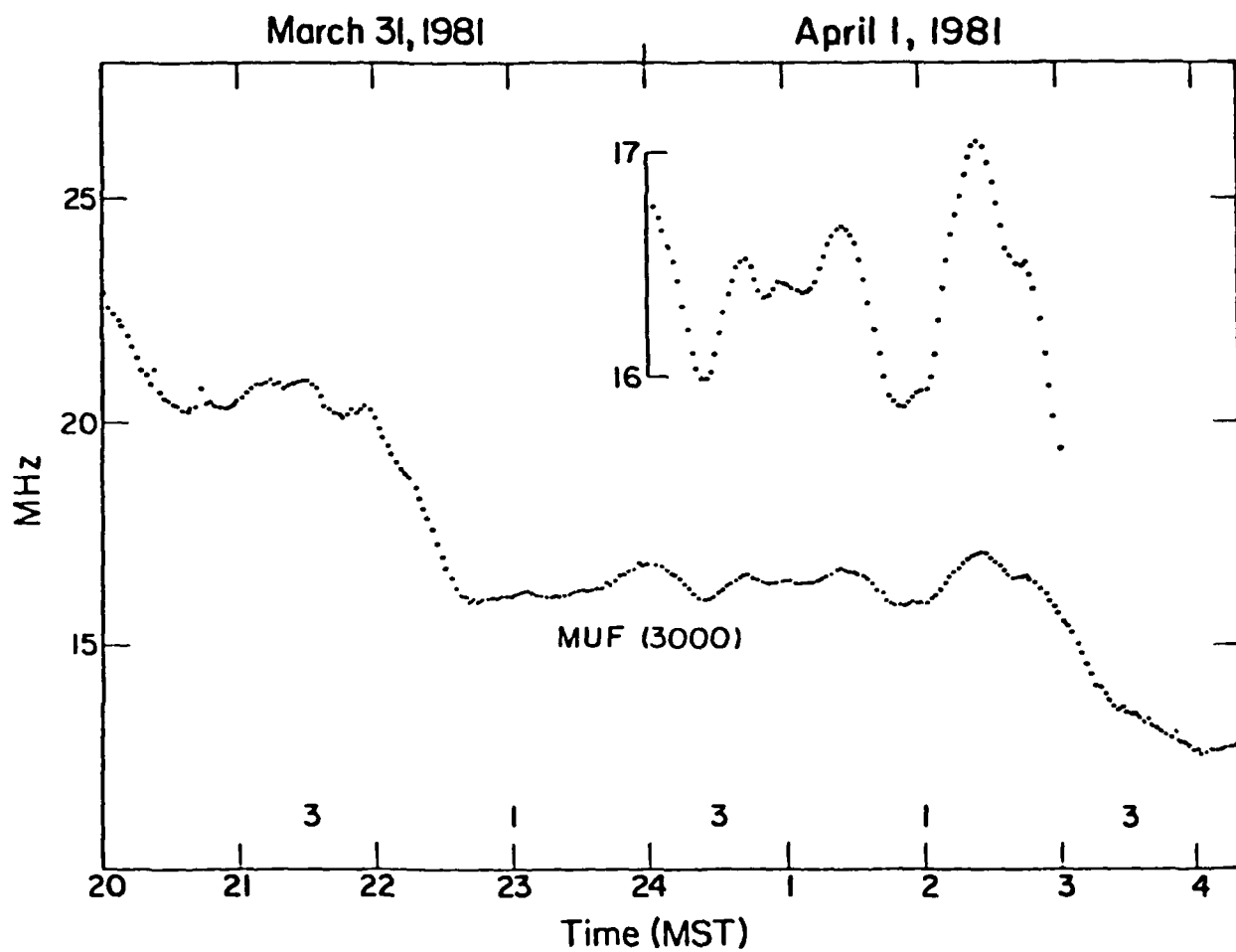


Figure 3. High-resolution temporal variation of MUF (3000).

Brighton, April 1, 1981

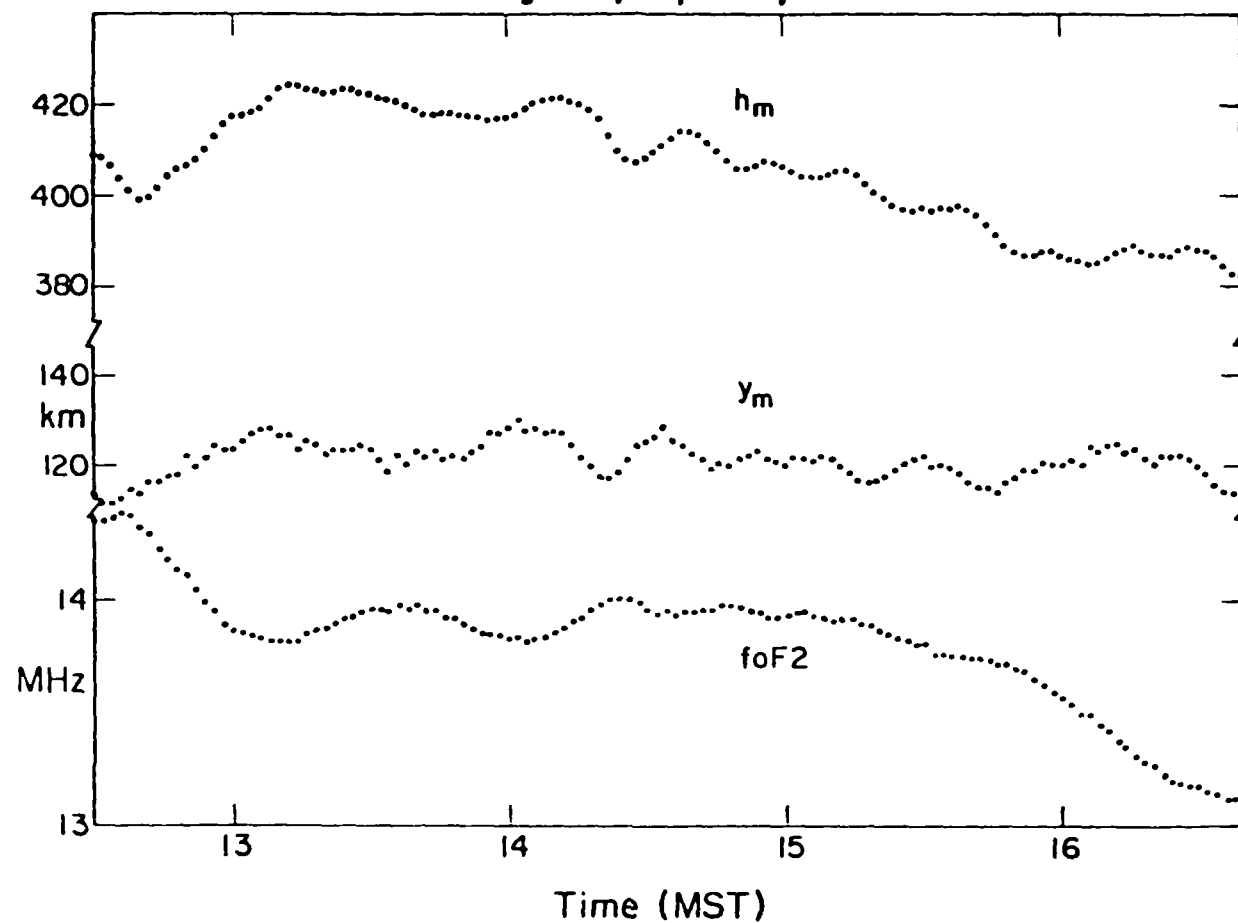


Figure 4. Temporal variation of height of maximum, half-thickness, and critical frequency of the F2 layer.

Brighton, March 25, 1981

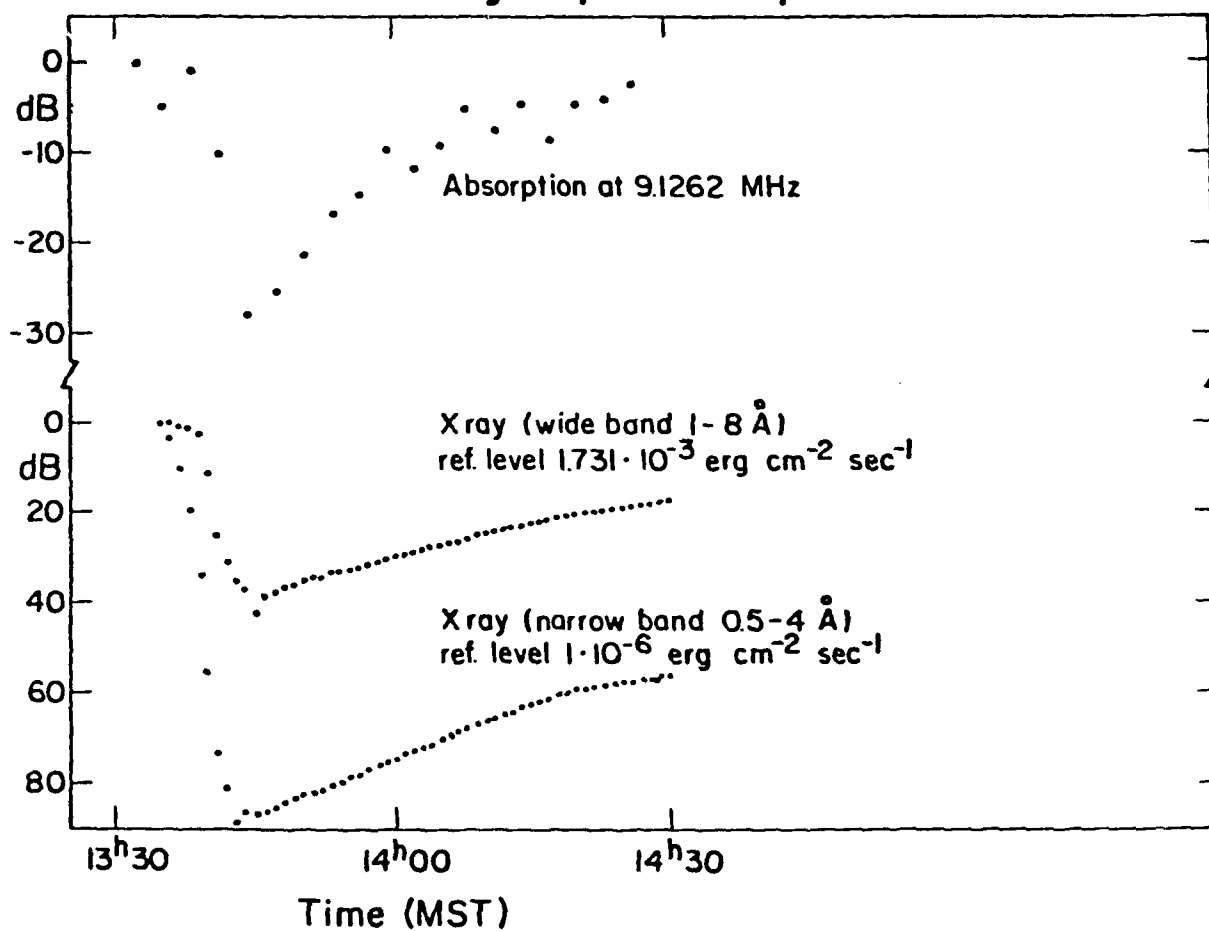


Figure 5. Comparison of absorption with X-ray flux during a solar flare.